

Turbulence in a Sheared, Salt-Fingering-Favorable Environment: Anisotropy and Effective Diffusivities

SATOSHI KIMURA AND WILLIAM SMYTH

College of Oceanic and Atmospheric Sciences, Oregon State University, Corvallis, Oregon

ERIC KUNZE

Applied Physics Laboratory, University of Washington, Seattle, Washington

(Manuscript received 5 August 2010, in final form 14 November 2010)

ABSTRACT

Direct numerical simulations (DNS) of a shear layer with salt-fingering-favorable stratification have been performed for different Richardson numbers Ri and density ratios R_ρ . In the absence of shear ($Ri = \infty$), the primary instability is square planform salt fingering, alternating cells of rising and sinking fluid. In the presence of shear, salt fingering takes the form of salt sheets, planar regions of rising and sinking fluid, aligned parallel to the sheared flow. After the onset of secondary instability, the flow becomes turbulent. The continued influence of the primary instability distorts the late-stage structure and hence biases isotropic estimates of the turbulent kinetic energy dissipation rate ϵ . In contrast, thermal and saline gradients evolve to become more isotropic than velocity gradients at their dissipation scales. Thus, the standard observational methodology of estimating the turbulent kinetic energy dissipation rate ϵ from vertical profiles of microscale gradients and assuming isotropy can underestimate its true value by a factor of 2–3, whereas estimates of thermal and saline dissipation rates using this approach are relatively accurate. Likewise, estimates of Γ from vertical profiles overestimate the true Γ by roughly a factor of 2. Salt sheets are ineffective at transporting momentum. Thermal and saline effective diffusivities decrease with decreasing Ri , despite the added energy source provided by background shear. After the transition to turbulence, the thermal to saline flux ratio and the effective Schmidt number remain close to the values predicted by linear theory.

1. Introduction

Salt-fingering-favorable stratification occurs when a gravitationally unstable vertical gradient of salinity is stabilized by that of temperature. In such conditions, the faster diffusion of heat relative to salt can generate cells of rising and sinking fluid known as salt fingers. Salt-fingering-favorable stratification is found in much of the tropical and subtropical pycnocline (You 2002). The most striking signatures are in thermohaline staircases, stacked layers of different water types separated by sharp thermal and saline gradient interfaces. These are found at several locations, such as in the subtropical confluence east of Barbados, under the Mediterranean and Red Sea salt

tongues, and in the Tyrrhenian Sea (Tait and Howe 1968; Lambert and Sturges 1977; Schmitt 1994).

Salt-fingering-favorable conditions can be created by large-scale vertical shears associated with the subinertial circulation (Schmitt 1990). Zhang et al. (1998) found a significant relationship between the formation of fingering-favorable conditions and large-scale vertical shear in a model of the North Atlantic.

In the presence of finescale shear such as that due to high-wavenumber near-inertial waves in the ocean, salt-fingering instability is supplanted by salt-sheet instability, alternating planar regions of rising and sinking fluid, aligned parallel to the sheared flow (Linden 1974). Although theories for the initial growth of salt-fingering and salt-sheet instabilities are well established (Stern 1960; Linden 1974; Schmitt 1979b; Kunze 2003; Smyth and Kimura 2007), the vertical fluxes of momentum, heat, and salt in the nonlinear regime are not well understood.

Dissipation rates of property variances in turbulent salt fingering can be measured in the ocean by microstructure

Corresponding author address: Satoshi Kimura, British Antarctic Survey, Madingley Road, High Cross, Cambridge CB3 0ET, United Kingdom.
E-mail: skimura04@gmail.com

profilers, but interpretation of these results has historically relied on Kolmogorov’s hypothesis of isotropic turbulence (Gregg and Sanford 1987; Lueck 1987; Hamilton et al. 1989; St. Laurent and Schmitt 1999; Inoue et al. 2008). Kolmogorov (1941) proposed that small-scale turbulence statistics are universal in the limit of high Reynolds number. According to this hypothesis, anisotropy of the energy-containing scales is lost in the turbulent energy cascade so that the small scales, where energy is finally dissipated, are statistically isotropic. The assumption of small-scale isotropy greatly simplifies both the theory and modeling of turbulence, as well as interpretation of microstructure measurements. Because the Reynolds number in oceanic salt-fingering systems is $O(10)$ (McDougall and Taylor 1984), the validity of this assumption is questionable. We will examine both mixing rates and the isotropy of the dissipation range in turbulent salt fingering by means of direct numerical simulations of diffusively unstable shear layers.

Estimates of dissipation rates, combined with the Osborn and Cox (1972) diffusivity model, furnish estimates of the effective diffusivities of heat, salt, and momentum. Effective diffusivities are used to parameterize turbulent fluxes in models of large-scale phenomena, ranging from finescale thermohaline intrusions (e.g., Toole and Georgi 1981; Walsh and Ruddick 1995; Smyth and Ruddick 2010) to basin-scale circulations (e.g., Zhang et al. 1998; Merryfield et al. 1999).

Effective diffusivities can be calculated directly from direct numerical simulations (DNS). Thermal and saline effective diffusivities for two-dimensional (2D) salt fingering have been computed in previous studies (W. J. Merryfield and M. Grindler 2000, personal communication; Stern et al. 2001; Yoshida and Nagashima 2003; Shen 1995). The effective diffusivities for 3D sheared salt fingering were first calculated by Kimura and Smyth (2007) for a single initial state.

In this paper and the companion paper (Smyth and Kimura 2011), we extend Kimura and Smyth (2007) to cover a range of oceanographically relevant initial background states. We focus on the case for which the Richardson number Ri exceeds the critical value $1/4$: that is, shear is too weak to produce Kelvin–Helmholtz instability (Miles 1961). The case $Ri < 1/4$ is addressed separately (Smyth and Kimura 2011). Although oceanic salt fingering does not always lead to staircases; that is the regime we focus on here as it is most amenable to direct simulation.

In section 2, we describe our DNS model and initial conditions. An overview of salt-sheet evolution is given in section 3. Section 4 discusses the nature of anisotropy at dissipation scales and its implications for interpreting profiler measurements. In section 5, we discuss the effective

diffusivities of momentum, heat, and salt and suggest a parameterization in terms of ambient property gradients. Our conclusions are summarized in section 6.

2. Methodology

We employ the three-dimensional incompressible Navier–Stokes equations with the Boussinesq approximation. The evolution equations for the velocity field, $\mathbf{u}(x, y, z, t) = (u, v, w)$, in a nonrotating, Cartesian coordinate system (x, y, z) are

$$\left[\frac{D}{Dt} - \nu \nabla^2 \right] \mathbf{u} = -\nabla \pi + b \mathbf{k} + \nu \nabla^2 \mathbf{u}$$

$$\nabla \cdot \mathbf{u} = 0. \tag{1}$$

Here, $D/Dt = \partial/\partial t + \mathbf{u} \cdot \nabla$ and ν are the material derivative and kinematic viscosity, respectively. The variable π represents the reduced pressure (pressure scaled by the uniform density ρ_0). The total buoyancy is defined as $b = -g(\rho - \rho_0)/\rho_0$, where g is the acceleration due to gravity. Buoyancy acts in the vertical direction, as indicated by the vertical unit vector \mathbf{k} . We assume that the equation of state is linear, and therefore the total buoyancy is the sum of thermal and saline buoyancy components (b_T and b_S), each governed by an advection–diffusion equation,

$$b = b_T + b_S;$$

$$\frac{Db_T}{Dt} = \kappa_T \nabla^2 b_T; \quad \text{and} \tag{2}$$

$$\frac{Db_S}{Dt} = \kappa_S \nabla^2 b_S. \tag{3}$$

Molecular diffusivities of heat and salt are denoted by κ_T and κ_S , respectively.

Periodicity intervals in streamwise x and spanwise y directions are L_x and L_y . The variable L_z represents the vertical domain length. Upper and lower boundaries, located at $z = -L_z/2$ and $z = L_z/2$, are impermeable ($w = 0$), stress free ($\partial u/\partial z = \partial v/\partial z = 0$), and insulating with respect to both heat and salt ($\partial b_T/\partial z = \partial b_S/\partial z = 0$).

To represent mixing in the high-gradient interface of a thermohaline staircase, we initialize the model with a stratified shear layer in which shear and stratification are concentrated at the center of the vertical domain with a half-layer thickness of h ,

$$\frac{u}{\Delta u} = \frac{b_T}{\Delta B_T} = \frac{b_S}{\Delta B_S} = \tanh\left(\frac{z}{h}\right).$$

The constants Δu , ΔB_T , and ΔB_S represent the change in streamwise velocity, thermal buoyancy, and saline

TABLE 1. Relevant parameters used in our DNS experiments. The wavenumber of the fastest-growing salt-fingering instability is determined by the magnitude of wavenumber, $k^2 + l^2$, where k and l represent the streamwise and spanwise wavenumbers. In the case of salt sheets (all cases except DNS5), there is not streamwise dependence ($k = 0$), where the salt-fingering case (DNS5) has $k = l$. In our DNS experiments, $k^2 + l^2$ is kept constant.

Case	1	2	3	4	5	6	7
Ri	0.5	2	6	20	∞	6	6
R_ρ	1.6	1.6	1.6	1.6	1.6	1.2	2.0
Pr	7	7	7	7	7	7	7
Re	1914	957	553	302	0	553	553
τ	0.04	0.04	0.04	0.04	0.04	0.04	0.04
λ_{fg} (m)	0.031	0.031	0.031	0.031	0.031	0.031	0.031
L_x (m)	0.9	0.9	0.9	0.9	1.2	0.9	0.9
L_y (m)	0.12	0.12	0.12	0.12	0.18	0.12	0.12
L_z (m)	1.8	1.8	1.8	1.8	1.8	1.8	1.8
nx	1024	1024	1024	1024	1024	1024	1024
ny	144	144	144	144	144	144	144
nz	2048	2048	2048	2048	1538	2048	2048

buoyancy across the half-layer thickness of h . For computational economy, we set $h = 0.3$ m, which is larger than the maximum finger height predicted by Kunze (1987). This is at the low end of the range of observed layer thickness (e.g., Gregg and Sanford 1987; Kunze 1994). The change in the total buoyancy is $\Delta B = \Delta B_T + \Delta B_S$. In all the DNS experiments, the initial interface buoyancy frequency $\sqrt{\Delta B}/h$ is fixed at $1.5 \times 10^{-2} \text{ rad s}^{-1}$, a value typical of the thermohaline staircase east of Barbados (Gregg and Sanford 1987). These constants can be combined with the fluid parameters ν , κ_T , and κ_S to form the following nondimensional parameters, which characterize the flow at $t = 0$:

$$\text{Ri} = \frac{\Delta B h}{\Delta u^2};$$

$$R_\rho = -\frac{\Delta B_T}{\Delta B_S};$$

$$\text{Pr} = \frac{\nu}{\kappa_T}; \quad \text{and}$$

$$\tau = \frac{\kappa_S}{\kappa_T}.$$

We have done seven experiments with different Ri and R_ρ (Table 1). The bulk Richardson number Ri measures the relative importance of stratification and shear. If $\text{Ri} < 0.25$, the initial flow is subjected to shear instabilities (Miles 1961; Howard 1961; Hazel 1972; Smyth and Kimura 2011). Here, we chose high enough Ri to ensure that shear instabilities do not disrupt the growth of salt-fingering modes. A typical range of Ri in a sheared thermohaline staircase is $\sim(3\text{--}100)$ (Gregg and Sanford 1987; Kunze 1994). The Reynolds number based on the half-layer thickness and the half change in streamwise velocity

is given by $\text{Re} = h\Delta u/\nu$. Because ΔB and h are kept constant in our simulations, Re and Ri are not independent: $\text{Re} = 1354\text{Ri}^{-1/2}$ with $\text{Re} = 0$ and $\text{Ri} = \infty$, representing a single unshered case that was included for comparison.

The density ratio R_ρ quantifies the stabilizing effect of thermal to destabilizing effect of saline buoyancy components; salt fingering grows more rapidly as R_ρ approaches unity. The value $R_\rho \approx 2$ is characteristic of the main thermocline in the subtropical gyres (Schmitt et al. 1987; Schmitt 2003). Thermohaline staircases form when R_ρ is less than 1.7 (Schmitt et al. 1987), and values as low as 1.15 have been reported (Molcard and Tait 1977). To cover this range of fingering regimes, we use the values 2, 1.6, and 1.2. The Prandtl number Pr and diffusivity ratio τ represent ratios of the molecular diffusivities of momentum, heat, and salt. The Prandtl number was set to 7, which is typical for seawater. The diffusivity ratio in the ocean is 0.01: that is, the heat diffuses two orders of magnitude faster than salt. The vast difference in diffusivity requires DNS to resolve a wide range of spatial scales, making it computationally expensive. In previous DNS of seawater, τ has been artificially increased to reduce computational expense (e.g., Stern et al. 2001; Gargett et al. 2003; Smyth et al. 2005). Kimura and Smyth (2007) conducted the first 3D simulation with $\tau = 0.01$ and found that increasing τ from 0.01 to 0.04 reduced thermal and saline effective diffusivities by one-half. In the cases presented here, we set τ to 0.04 to allow extended exploration of the Ri and R_ρ dependence.

The fastest-growing salt-sheet wavelength predicted by linear stability analysis is $\lambda_{fg} = 2\pi(\nu k_T 2h/\Delta B)^{1/4}$ (Stern 1975; Schmitt 1979b). Our value of $\lambda_{fg} = 0.032$ m is similar to the observed wavelength (Gregg and Sanford 1987; Lueck 1987). We accommodate four wavelengths of the fastest-growing primary instability in the spanwise

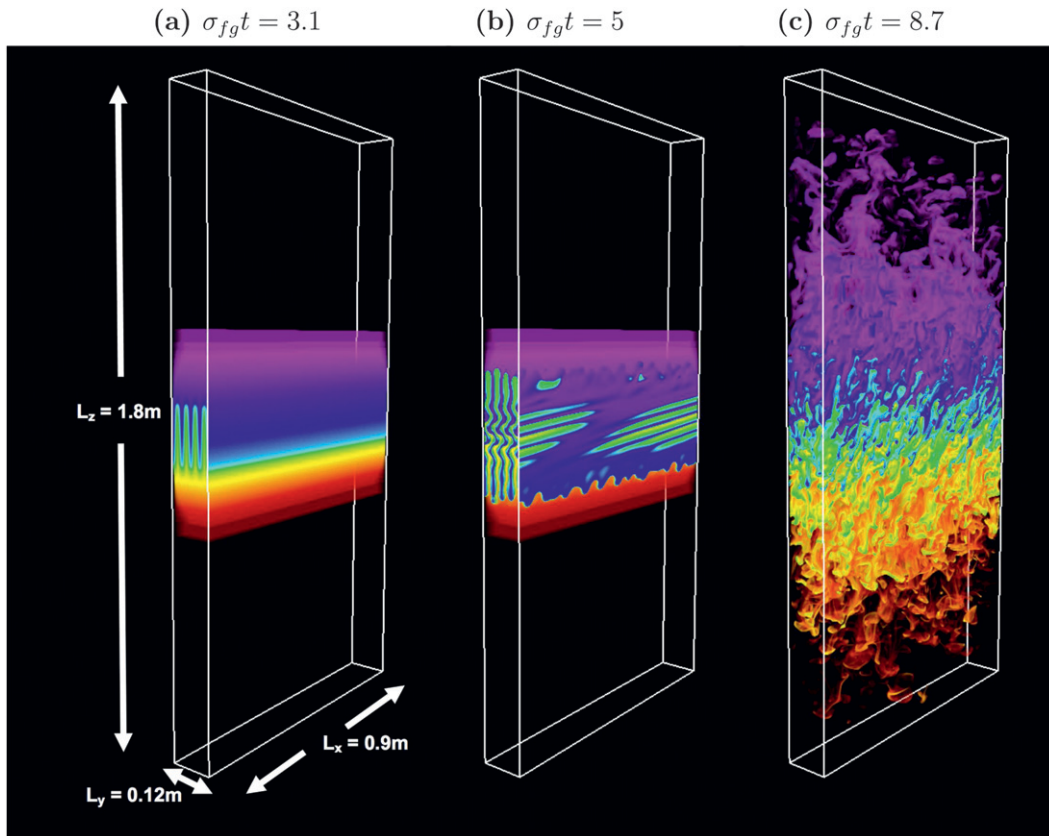


FIG. 1. Evolution of saline buoyancy field for $Ri = 6$, $R_p = 1.6$ in an interface sandwiched between two homogeneous layers: $\sigma_{fst} =$ (a) 3.1, (b) 5, and (c) 8.7. Inside the interface, the lowest ($-7.15 \times 10^{-5} \text{ m}^2 \text{ s}^{-1}$) and highest ($7.15 \times 10^{-5} \text{ m}^2 \text{ s}^{-1}$) saline buoyancy are indicated by purple and red, respectively. Homogeneous regions above and below the high-gradient layer are transparent.

direction, $L_y = 4\lambda_{fg}$. The vertical domain length L_z was chosen such that vertically propagating plumes reach statistical equilibrium; we found that L_z equal to 6 times h was sufficient. Here, L_x was chosen to be large enough to accommodate subsequent secondary instabilities. After sensitivity tests, we chose $L_x = 28\lambda_{fg}$.

The primary instability was seeded by adding an initial disturbance proportional to the fastest-growing mode of linear theory, computed numerically as described in Smyth and Kimura (2007). We seed square planforms for the unsheared case and sheets in the presence of shear. The vertical displacement amplitude is set to $0.02h$, and a random noise is added to the initial velocity field with an amplitude of $1 \times 10^{-2} h\sigma_{fg}$ to seed secondary instabilities. The variable σ_{fg} indicates the growth rate of the fastest-growing linear normal mode.

The numerical code used to solve (1)–(3) is described by Winters et al. (2004). The code uses Fourier pseudo-spectral discretization in all three directions and time integration using a third-order Adams–Bashforth operator. A time step is determined by a Courant–Friedrichs–Lewy

(CFL) stability condition. The CFL number is maintained below 0.21 for DNS experiments presented here. The code was modified by Smyth et al. (2005) to accommodate a second active scalar, which is resolved on a fine grid with spacing equal to $\frac{1}{2}$ the spacing used to resolve the other fields. The fine grid is used to resolve salinity. The fine-grid spacing is equal to $0.15\lambda_{fg}\sqrt{\tau}$ in all three directions, as suggested by Stern et al. (2001).

3. Simulation overview

Figure 1 shows the saline buoyancy field for the case $Ri = 6$, $R_p = 1.6$ at selected times. The time is scaled by the linear normal growth rate of salt sheets σ_{fg} described by Smyth and Kimura (2007). Figure 1a shows the salt-sheet instability: the planar regions of vertical motions oriented parallel to the background shear flow. Rising and sinking fluid appear in green and blue, respectively.

When the salt sheets reach the edges of the interface (indicated by purple and red), they start to undulate in the spanwise direction (Fig. 1b). At the same time, the

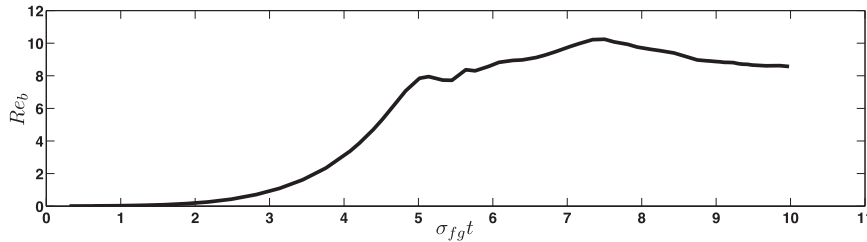


FIG. 2. Evolution of volume-averaged Re_b for $Ri = 6$, $R_\rho = 1.6$. After initial roughly exponential growth, Re_b reaches a statistical steady state after $\sigma_{fg}t \sim 5$.

salt sheets develop streamwise dependence at the edges and center of the interface. At the edges of the interface, the streamwise dependence appears as ripples. At the center, tilted laminae are evident, reminiscent of those seen in shadowgraph images of optical microstructure (Kunze 1987, 1990; St. Laurent and Schmitt 1999). After the salt sheets are disrupted, the flow evolves into turbulent salt fingering (Fig. 1c).

4. Dissipation rates and isotropy

In this section, we explore the geometry of scalar (thermal and saline buoyancy) and velocity gradient fields. The isotropy of scalar fields is diagnosed in terms of the thermal and saline buoyancy variance dissipation rates,

$$\chi_T = 2\kappa_T \langle |\nabla b'_T|^2 \rangle; \quad \chi_S = 2\kappa_S \langle |\nabla b'_S|^2 \rangle. \quad (4)$$

Variables, b'_T and b'_S are thermal and saline buoyancy perturbations,

$$b'_T(x, y, z, t) = b_T(x, y, z, t) - B_T(z, t) \quad \text{and}$$

$$b'_S(x, y, z, t) = b_S(x, y, z, t) - B_S(z, t),$$

where B_T and B_S are horizontally averaged b_T and b_S , respectively. The angle brackets indicate averaging over volume between $-2h < z < 2h$, where turbulent salt fingering is most active.

Turbulent kinetic energy dissipation rate is given by

$$\epsilon = \frac{\nu}{2} \left\langle \left(\frac{\partial u'_i}{\partial x_j} + \frac{\partial u'_j}{\partial x_i} \right)^2 \right\rangle.$$

The primes indicate the perturbation velocity fields,

$$\mathbf{u}'(x, y, z, t) = \mathbf{u}(x, y, z, t) - [U(z, t), 0, 0], \quad (5)$$

where $U(z, t)$ is the streamwise velocity averaged over horizontal directions.

In shear-driven turbulence, the degree of isotropy is predicted by the buoyancy Reynolds number, $Re_b = \epsilon/\nu N^2$, where $N^2 = \langle B_{T,z} + B_{S,z} \rangle$. Subscripts preceded by commas indicate partial differentiation. As Re_b increases, the dissipation range separates from the energy-containing scales and become increasingly isotropic. Gargett et al. (1984) concluded from observations of shear-driven turbulence that ϵ can be accurately estimated based on isotropy when $Re_b > 2 \times 10^2$. Itsweire et al. (1993) found that the assumption of isotropy is invalid for $Re_b < 10^2$ using DNS of a uniformly stratified shear flow. A similar result holds in DNS of a localized stratified shear layer (Smyth and Moum 2000). The skill of Re_b as a predictor of isotropy in turbulent salt fingering remains to be assessed.

In fingering-favorable stratification with turbulence, laboratory experiments have shown that finger structures have $Re_b \sim O(10)$ for $R_\rho < 2$ (McDougall and Taylor 1984). Oceanic observations also suggest that $Re_b \sim O(10)$ (St. Laurent and Schmitt 1999; Inoue et al. 2008). The Re_b from our simulation increases until salt sheets start to break up ($\sigma_{fg}t \approx 5$) and reaches a maximum value of $Re_b = 10.8$ at $\sigma_{fg}t = 8$ (Fig. 2). After $\sigma_{fg}t > 8$, the flow becomes quasi steady with $Re_b \approx 10$.

In our DNS, Re_b is comparable to the observed values quoted above; therefore, we may use our results to quantify the bias inherent in one-dimensional observational estimates of dissipation rates. Although the criterion found for shear-driven turbulence that dissipation-scale isotropy occurs above $Re_b \sim 200$ does not apply directly to turbulent salt fingering, the relatively small value for Re_b found in both DNS and observations suggests that the dissipation scales could be significantly anisotropic.

a. Isotropic approximations for χ_S and χ_T

Most oceanographic microstructure measurements are one dimensional, either in the vertical or horizontal, and assume isotropy in estimating dissipation rates. The validity of this assumption is tested here for turbulent salt fingering. The saline and thermal variance dissipation rates can be expressed in three different forms as

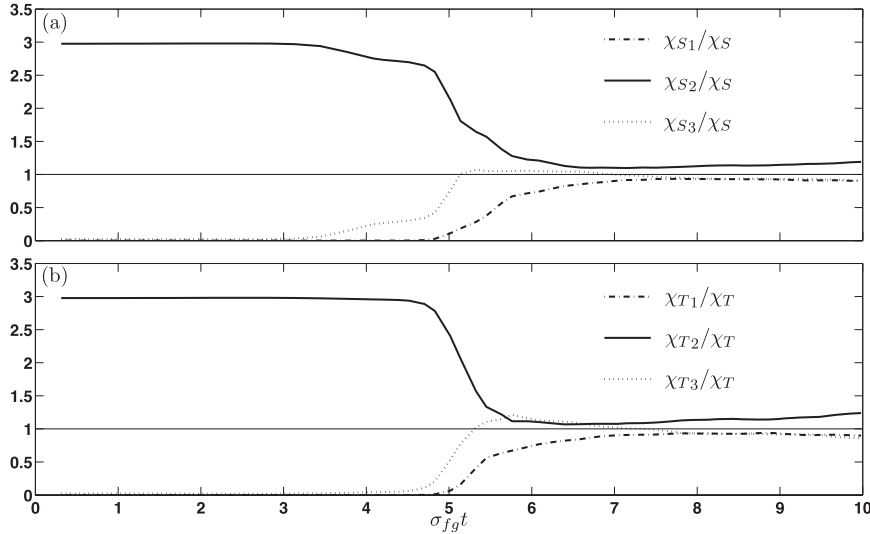


FIG. 3. (a) Saline and (b) thermal buoyancy variance dissipation rates computed from individual derivatives (χ_{S_i} and χ_{T_i}) represented as fractions of the true value (χ_S and χ_T) for the case $Ri = 6$, $R_\rho = 1.6$. The solid horizontal lines indicate unity (the ratio for isotropic turbulence).

$$\chi_{S_i} = 6\kappa_S \left\langle \left(\frac{\partial b'_S}{\partial x_i} \right)^2 \right\rangle \quad \text{and} \quad (6)$$

$$\chi_{T_i} = 6\kappa_T \left\langle \left(\frac{\partial b'_T}{\partial x_i} \right)^2 \right\rangle, \quad (7)$$

where i ranges from 1 to 3 and is not summed over. Each of three different forms has the same magnitude for isotropic turbulence (e.g., $\chi_S = \chi_{S_1} = \chi_{S_2} = \chi_{S_3}$). Despite $Re_b \sim O(10)$ for observed salt fingering, observations and numerical simulations support the thermal buoyancy field being nearly isotropic. Two-dimensional numerical simulations of Shen (1995) showed that the thermal spectral variance is distributed approximately equally in both vertical and horizontal wavenumbers. Lueck (1987) found that the magnitude of the vertical thermal buoyancy gradient was similar to the horizontal gradient in a thermocline staircase east of Barbados. Because the measurements were taken at sites with $Ri \sim 10$ and never less than unity, Lueck (1987) argued that the isotropic structure is not likely the result of shear-driven turbulence. Shadowgraph images of salt fingering showed coherent tilted laminae (Kunze 1987). Because shadowgraph images tend to emphasize the dissipative scales of the salinity field, the shadowgraph images are thought to reflect anisotropic salinity structures at the salinity Batchelor scale (Kunze 1987, 1990; St. Laurent and Schmitt 1999).

In our simulations, signatures of salt-sheet anisotropy decrease with time in both saline and thermal buoyancy

fields (Figs. 3a,b). In the linear regime ($0 < \sigma_{fg}t < 3$), virtually all salinity and thermal buoyancy variance dissipation comes from spanwise derivatives (indicated by solid lines in Figs. 3a,b), consistent with the geometry of salt sheets. With the onset of secondary instability, contributions from streamwise and vertical derivatives increase. The ratios χ_{S_i}/χ_S and χ_{T_i}/χ_T become quasi steady in the turbulent regime ($\sigma_{fg}t > 8$), by which time temperature and salinity structure are nearly isotropic. The slight ($\sim 10\%$) anisotropy that remains in the turbulent state is consistent with that of the initial instability, with the contribution from the spanwise derivative being the largest. Even after transition, salt-fingering-favorable mean stratification is maintained and salt-sheet instability continues to influence small-scale anisotropy.

We now turn to the effects of Ri and R_ρ on isotropy, focusing on the thermal buoyancy because it is easiest to measure in the ocean. Time averages of the ratios χ_{T_i} over $\sigma_{fg}t > 8$ succinctly represent the Ri and R_ρ dependences of anisotropy in the turbulent state (Fig. 4). As in Fig. 3, anisotropy characteristics of the linear instability are evident in the turbulent regime (Fig. 4a). In the unsheared case $Ri = \infty$, the contributions from the horizontal derivatives are approximately equal ($\chi_{T_1} \approx \chi_{T_2}$), indicating that the thermal buoyancy gradient is statistically axisymmetric about the vertical. As Ri decreases (i.e., as background shear is increased from zero), the contribution from χ_{T_2} increases, whereas that from χ_{T_1} decreases. The contribution from χ_{T_3} to χ_T increases with decreasing Ri , resembling the characteristics of

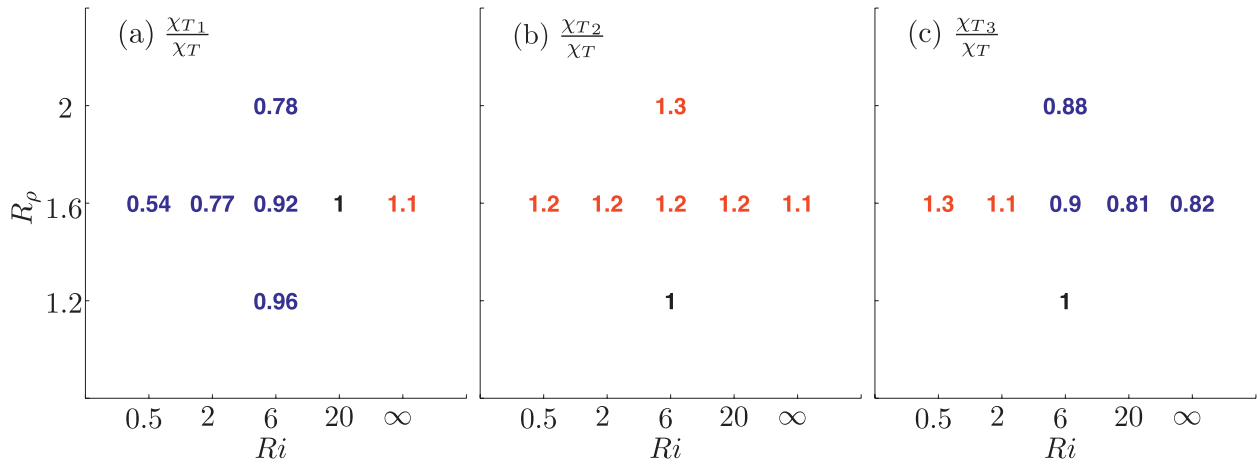


FIG. 4. Approximate average ratios of component thermal variance dissipation rates with the true dissipation rates χ_{T_i}/χ_T for various Ri and R_ρ : (a) χ_{T1}/χ_T , (b) χ_{T2}/χ_T , and (c) χ_{T3}/χ_T . Each of the three different forms in (7) is normalized by its true value χ_T to quantify the degree of anisotropy. Each ratio is averaged for $\sigma_{igt} > 8$ to represent the properties of the turbulent state. Ratios below unity are blue, ratios above unity are red, and ratios equal to unity are black.

shear-driven turbulence (Itsweire et al. 1993; Smyth and Moum 2000).

As R_ρ increases, the geometric characteristics of salt sheets dominate (Fig. 4b); that is, the contribution from χ_{T2} increases with increasing R_ρ , whereas the contribution from χ_{T1} decreases. Salt sheets become more horizontally isotropic ($\chi_{T1} \approx \chi_{T2}$) with decreasing R_ρ (Fig. 4b), as observed in laboratory salt-fingering experiments (Taylor 1992). Furthermore, isotropy approximations become more accurate with decreasing R_ρ (Figs. 4a–c), which also holds in DNS of three-dimensional unbounded salt fingers (Caplan 2008).

b. Isotropic approximations for ϵ

In isotropic turbulence, ϵ can be represented by any one of the nine expressions,

$$\epsilon = \frac{15\nu}{2 - \delta_{ij}} \left\langle \left(\frac{\partial u'_i}{\partial x_j} \right)^2 \right\rangle, \quad (8)$$

with no summation over i or j (Taylor 1935). The variable δ_{ij} represents the Kronecker delta function. In general, these expressions are unequal, and their differences reflect the degree of anisotropy of the velocity gradients at dissipation scales.

We look first at expressions involving the three derivatives of the vertical velocity, because these will prove to dominate. In the unsheared case (Fig. 5a), the contribution from w'_{y2} and w'_{x2} are the same, reflecting the geometry of salt-fingering instability. In the sheared case (Fig. 5b), the contributions from cross-sheet w'_{y2} to ϵ exceed those of along-sheet w'_{x2} and vertical w'_{z2} , reflecting the geometry

of salt-sheet instability. As the flow becomes turbulent, the ratios $7.5\nu\langle w'_{x2} \rangle/\epsilon$, $7.5\nu\langle w'_{y2} \rangle/\epsilon$, and $7.5\nu\langle w'_{z2} \rangle/\epsilon$ reach steady values between 1.5 and 3 at $\sigma_{igt} \approx 8$ (Figs. 5a,b); however, none of the ratios converge to unity. The axisymmetry of the primary salt-fingering state continues to influence the geometry of the dissipation scales in the turbulent state (Fig. 5a). In contrast, the geometry of the salt-sheet instability is disrupted by the increase in contribution from w'_{x2} in the turbulent state (Fig. 5b).

To quantify Ri and R_ρ dependence, the nine approximations in (8) were averaged over $\sigma_{igt} > 8$ and normalized by the true value of ϵ in the turbulent regime (Fig. 6). Approximations involving the vertical velocity all overestimate ϵ , as illustrated previously in Fig. 5, whereas those involving horizontal velocities underestimate ϵ . This is consistent with the dominance of vertical motions in turbulent salt fingers and salt sheets. In the absence of background shear, the contributions from w'_{x2} and w'_{y2} are the largest, which is consistent with the horizontal isotropy of square planform salt fingering. In the sheared cases, the contribution from w'_{y2} is the largest, consistent with salt-sheet geometry, but, unlike in the linear regime, the contribution from w'_{x2} is significant.

In both sheared and unsheared cases, the second largest contribution comes from w'_{z2} . This vertical convergence squeezes the fluid vertically at the tips of rising and sinking plumes. This vertical compression is compensated by horizontal divergence ($\langle w'_{z2} \rangle \approx \langle u'_{x2} \rangle, \langle v'_{y2} \rangle$). Because of the difference in geometry between sheared and unsheared cases, the contributions from u'_{x2} and v'_{y2} that balance w'_{z2} differ. In the unsheared case, the vertically squeezed fluid at the tips of plumes is displaced equally in the streamwise and spanwise directions ($\langle u'_{x2} \rangle \approx \langle v'_{y2} \rangle$). In

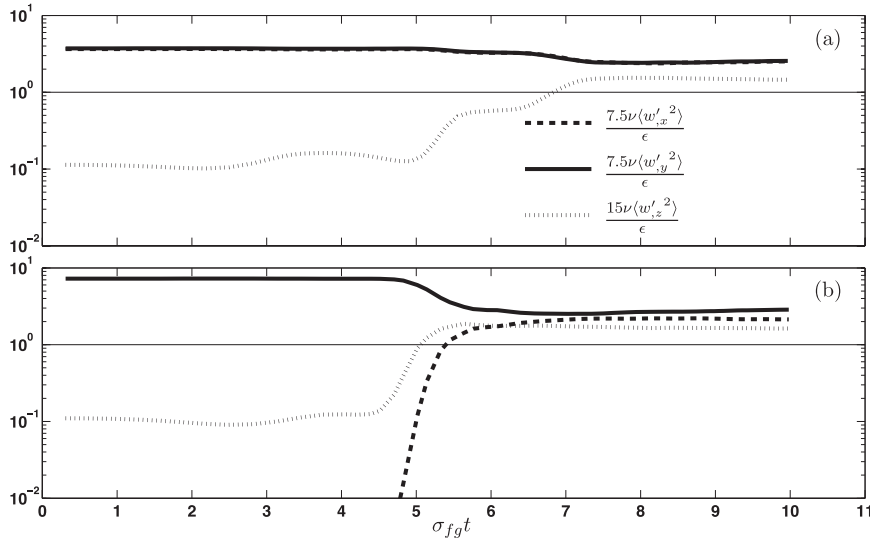


FIG. 5. Evolution of component ratios $7.5\nu\langle w'^2_{x,x} \rangle/\epsilon$, $7.5\nu\langle w'^2_{y,y} \rangle/\epsilon$, and $7.5\nu\langle w'^2_{z,z} \rangle/\epsilon$ for (a) un-sheared case ($Ri = \infty, R_\rho = 1.6$) and (b) sheared case ($Ri = 6, R_\rho = 1.6$). The solid horizontal lines indicate the ratio for isotropic turbulence ($=1$).

contrast, the geometry of the sheared case displaces more fluid in the spanwise direction ($\langle u'^2_{,x} \rangle < \langle v'^2_{,y} \rangle$).

The approximations using horizontal shears also show the influence of the linear instabilities. The balances

in the un-sheared case, $\langle u'^2_{,y} \rangle \approx \langle v'^2_{,x} \rangle$, $\langle u'^2_{,x} \rangle \approx \langle v'^2_{,y} \rangle$, and $\langle u'^2_{,z} \rangle \approx \langle v'^2_{,z} \rangle$, indicate axisymmetry about the vertical.

As Ri decreases, contributions from $u'^2_{,z}$ and $v'^2_{,z}$ increase. This indicates that the flow is developing characteristics

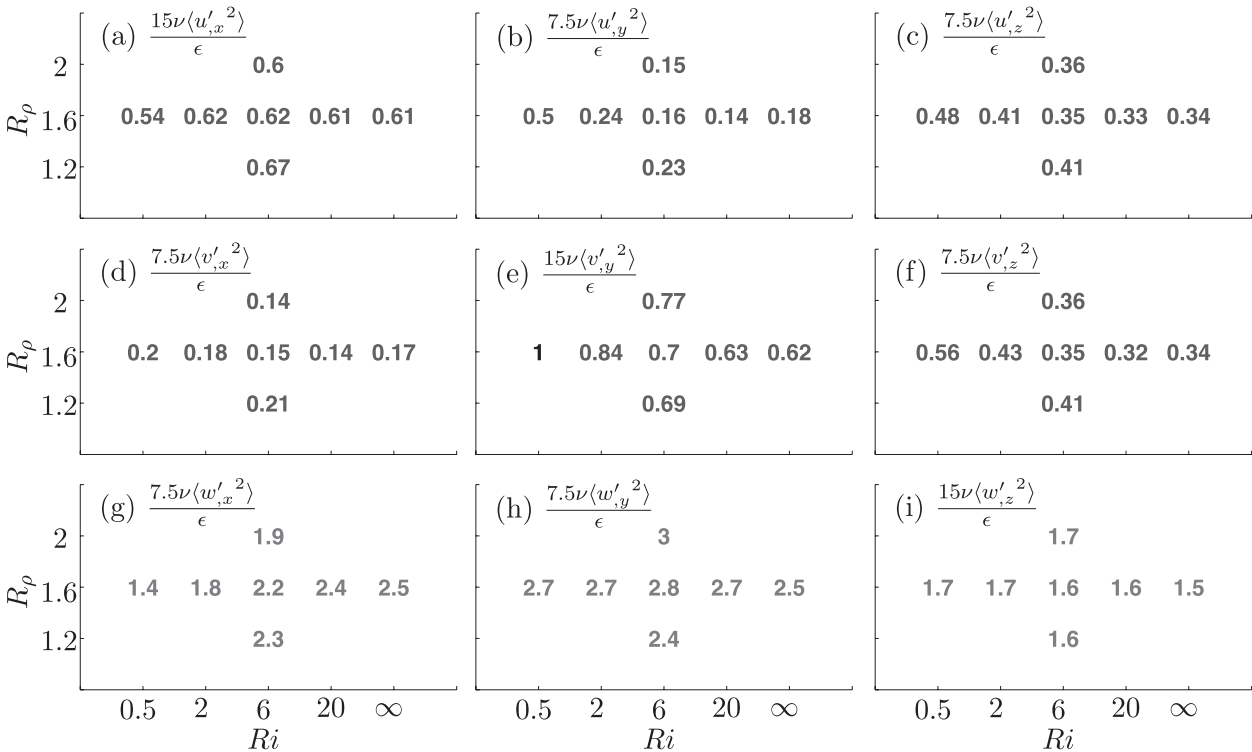


FIG. 6. Approximations of ϵ from each of the squared perturbation velocity derivatives as a fraction of its true value ϵ for different Ri and R_ρ . Each ratio is averaged for $\sigma_{fg}t > 8$ to represent the geometry in the turbulent state: for (a)–(c) u' , (d)–(f) v' , and (g)–(i) w' .

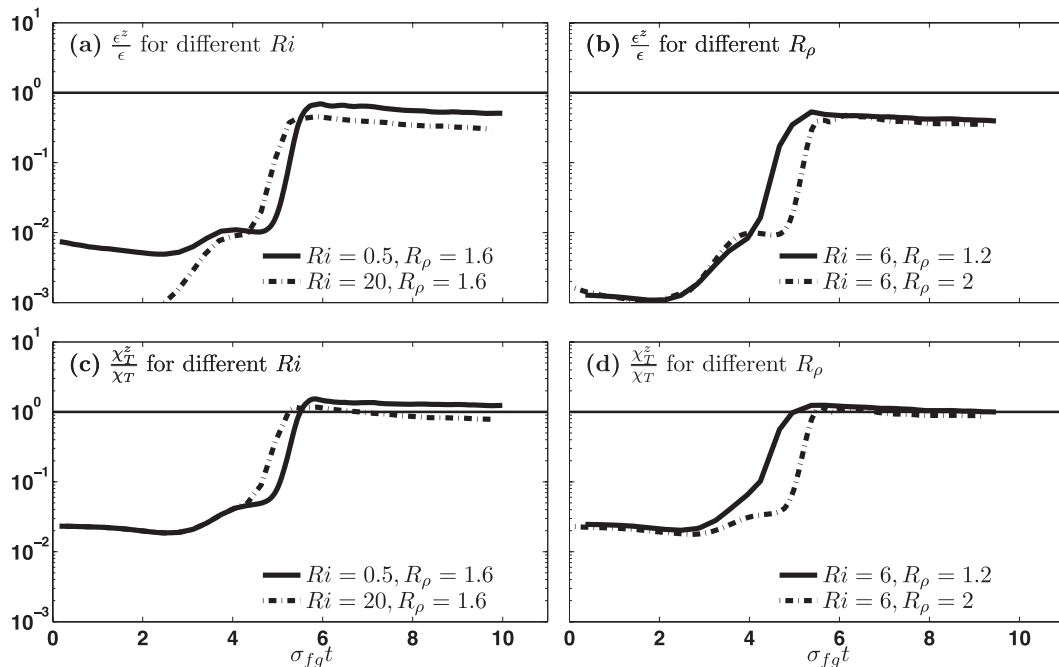


FIG. 7. Time evolution of the 1D vertical dissipation rates normalized by their true values. The ϵ^z/ϵ evolution is shown for different (a) Ri and (b) R_ρ . The χ_T^z/χ_T evolution is shown for different (c) Ri and (d) R_ρ . The solid horizontal lines indicate the ratio for isotropic turbulence.

of shear-driven turbulence as described by Itsweire et al. (1993) and Smyth and Moum (2000).

c. Impact of anisotropy on ϵ and χ_T from vertical profilers

Observational estimates of turbulent kinetic energy and thermal variance dissipation rates are often based on data from vertical profilers. Estimates of the salinity variance dissipation rate are scarce because of the need for extremely fine resolution (e.g., Nash and Moum 1999). The profilers measure the vertical change of horizontal velocities and temperature for which ϵ and χ_T are estimated by

$$\epsilon^z = \frac{15\nu}{4} \left\langle \left\langle \left(\frac{\partial u'}{\partial z} \right)^2 \right\rangle \right\rangle + \left\langle \left\langle \left(\frac{\partial v'}{\partial z} \right)^2 \right\rangle \right\rangle \quad \text{and} \quad (9)$$

$$\chi_T^z = 6\kappa_T \left\langle \left\langle \left(\frac{\partial b_T'}{\partial z} \right)^2 \right\rangle \right\rangle. \quad (10)$$

For isotropic flows, these approximations are exact: that is, $\epsilon = \epsilon^z$ and $\chi_T = \chi_T^z$. Though Re_b associated with fingering is $\sim(10)$, isotropic approximations have been justified by observations (Lueck 1987) and numerical simulation (Shen 1995), both showing nearly isotropic thermal buoyancy field in the turbulent regime. However, isotropy in temperature gradient does not guarantee

isotropy in velocity gradients. Furthermore, this justification does not hold for the initial stage of the flow when salt sheets or salt fingers are active. The geometry of salt fingers and salt sheets led theoretical models to utilize the “tall fingers” (TF) approximation in an unbounded salt fingers and salt sheets (Stern 1975; Kunze 1987; Smyth and Kimura 2007). Because salt fingers and salt sheets are tall and narrow, the TF approximation assumes that the vertical derivative is negligible relative to horizontal derivatives ($\epsilon^z = \chi_T^z = 0$).

The approximation (9) gives a poor estimate of ϵ , even in the turbulent regime of fingering (Figs. 7a,b). As the flow evolves, ϵ^z/ϵ increases from near zero but never converges to unity. Instead, at quasi-steady state, the ratio ranges between 0.32 and 0.52 for $\sigma_{fg}t > 8$ (Figs. 7a,b). In contrast, the quasi-steady value of χ_T^z/χ_T ranges between 0.8 and 1.2 (Figs. 7c,d). These results suggest that, in the presence of turbulent salt fingering, χ_T^z is an appropriate approximation, but ϵ^z underestimates ϵ by a factor of 2–3.

5. Turbulent fluxes and diffusivities

Of primary interest to the oceanographic community is understanding the turbulent fluxes associated with salt fingers. Measurements of ϵ and χ_T allow indirect estimates of turbulent fluxes via the dissipation ratio (also called “mixing efficiency”; e.g., McEwan 1983),

$$\Gamma = \frac{N^2 \chi_T}{2\epsilon \langle B_{T,z}^2 \rangle}. \quad (11)$$

$$\Gamma = \frac{R_\rho - 1}{R_\rho} \frac{\gamma_s}{1 - \gamma_s} \quad (14)$$

In turbulence, mechanical energy can be expended by raising the mass of fluid through mixing or kinetic energy dissipation by molecular viscosity. The quantity Γ approximates the fraction of the turbulent kinetic energy that is irreversibly converted to potential energy due to mixing. In shear-driven turbulence, Γ can be used to estimate the effective diffusivity of heat and salt as $K_T = K_S = \Gamma(\epsilon/N^2)$ (Osborn 1980).

The effective diffusivities of heat, salt, and momentum are defined via the standard flux–gradient relations,

$$K_T = -\frac{\langle w'b'_T \rangle}{\langle \frac{\partial B_T}{\partial z} \rangle}; \quad K_S = -\frac{\langle w'b'_S \rangle}{\langle \frac{\partial B_S}{\partial z} \rangle}; \quad K_U = -\frac{\langle u'w' \rangle}{\langle \frac{\partial U}{\partial z} \rangle}. \quad (12)$$

Relationships between the thermal and saline buoyancy and momentum fluxes can be expressed using the heat–salt flux ratio and the turbulent Schmidt number,

$$\gamma_s = -\frac{\langle w'b'_T \rangle}{\langle w'b'_S \rangle}; \quad \text{Sc} = \frac{K_U}{K_S}.$$

In square and sheet planform salt-fingering instabilities, an unstable distribution of mean saline buoyancy drives salt and heat fluxes downward. This implies that thermal buoyancy flux is working against the gravity, $w'b'_T < 0$. The turbulent Schmidt number quantifies the relative importance of effective diffusivity of momentum to that of salt. In the following subsections, we will quantify the Ri and R_ρ dependences of Γ , the effective diffusivities, γ_s , and Sc .

a. Estimation of Γ

The value of Γ can be approximated by Γ^z ,

$$\Gamma^z = \frac{N^2 \chi_T^z}{2\epsilon^z \langle B_{T,z}^2 \rangle}. \quad (13)$$

In homogeneous, stationary isotropic turbulence, $\Gamma = \Gamma^z$. In shear-driven turbulence, measurements indicate $\Gamma^z \approx 0.2$ (Osborn 1980; Oakey 1982; Moum 1996). This value is accurate for $\text{Re}_b > 2 \times 10^2$ (Gargett et al. 1984). Fastest-growing salt-finger theory suggests $0.2 < \Gamma^z < 0.8$ (Hamilton et al. 1989; Inoue et al. 2008), whereas measurements suggest that Γ can have higher values: $0.4 < \Gamma^z < 2$ (St. Laurent and Schmitt 1999; Inoue et al. 2008). At statistical steady state, balances of turbulent kinetic energy and scalar variance imply

in the absence of shear (Hamilton et al. 1989; McDougall and Ruddick 1992). For fastest-growing fingers, Γ can be expressed as a function of R_ρ by substituting $\gamma_s = (R_\rho)^{1/2}[(R_\rho)^{1/2} - (R_\rho - 1)^{1/2}]$ (Stern 1975; Kunze 1987). In the presence of shear, for the fastest-growing salt sheets,

$$\Gamma = \frac{R_\rho - 1}{R_\rho} \frac{\text{PrRi}}{\text{PrRi} + 1} \quad (15)$$

(Smyth and Kimura 2007). In the present DNS for $R_\rho = 1.6$, Γ lies below 0.6 (Fig. 8a). In the linear regime ($\sigma_{\text{fig}t} < 2$), Γ is consistent with (15). The value of Γ decreases slowly as the flow becomes unstable to secondary instability ($\sigma_{\text{fig}t} \sim 3$) and then becomes quasi steady between 0.3 and 0.4 in the turbulent salt-fingering regime.

The value of Γ^z is generally larger than Γ (Fig. 8b), consistent with $\epsilon^z < \epsilon$. For $\text{Ri} > 6$, Γ^z can be 30 times larger than Γ in the preturbulent state ($0 < \sigma_{\text{fig}t} < 3$). A local peak of Γ^z/Γ occurs during the secondary instability ($\sigma_{\text{fig}t} \sim 5$). As the flow becomes turbulent, the ratio decreases and approaches a quasi-steady value of ~ 2 : that is, Γ^z overestimates Γ by a factor of 2 in the turbulent salt-fingering regime.

Because both Γ and Γ^z become quasi steady after $\sigma_{\text{fig}t} = 8$, both Γ and Γ^z are averaged over $\sigma_{\text{fig}t} > 8$ to quantify Ri and R_ρ dependences in the turbulent regime. In all cases, Γ^z coincides approximately with observations (Fig. 9). Both observed and simulated Γ^z increase with increasing Ri . Similarly, Γ increases with increasing Ri . The R_ρ dependence of the observed Γ^z and the DNS result exhibit different trends (Fig. 10). Observed Γ^z decreases with increasing R_ρ , whereas both Γ^z and Γ from DNS increase with increasing R_ρ . The difference in R_ρ dependence of the observations and our simulation can be attributed to Ri . Our simulation has uniform Ri , whereas the Ri in the observation lies between 3 and 7. The linear result (15) from Smyth and Kimura (2007) predicts Γ from DNS remarkably well (Figs. 9, 10).

Our results contradict the isotropy assumption used to infer Γ from microstructure profiles. This has implications for recent attempts to extend the k – ϵ formalism to include double diffusion (Canuto et al. 2008), where Γ^z was used to validate model parameters. Also, Inoue et al. (2008) used Γ^z from St. Laurent and Schmitt (1999) to suggest that the wavelength of oceanic fingers is larger than that of the fastest-growing mode (their Fig. 5). In contrast, we find Γ consistent with linear fastest-growing fingers (Figs. 9, 10).

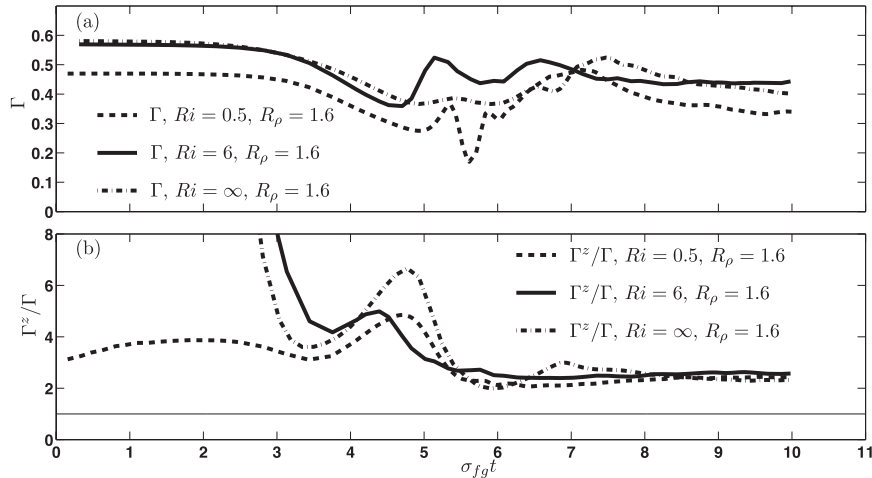


FIG. 8. Evolution of (a) Γ and (b) Γ^z normalized by its true value Γ for different Ri . These ratios are unity [thin solid line in (b)] for isotropic turbulence.

b. Effective diffusivities

Effective diffusivities are often used in large-scale models to represent small-scale physics (e.g., Bryan 1987; Gargett and Holloway 1992; Walsh and Ruddick 1995). Gargett and Holloway (1992) found that steady-state solutions of low-resolution general circulation models (GCMs) were sensitive to the ratio of K_T to K_S . More recent modeling studies have found that regional circulations are significantly altered when parameterizations of K_T and K_S due to fingering are introduced (Merryfield et al. 1999; Zhang et al. 1998).

Parameterizations of these diffusivities are essential in modeling flows where turbulent salt fingering controls small-scale fluxes of heat and salt, such as thermohaline interleaving. Walsh and Ruddick (2000) employed a parameterization of K_S for pure salt fingering, $K_S = K_{S_0} R_\rho^{-n}$. Smyth (2008) fitted this simple model to DNS results from Stern et al. (2001) and obtained $n = 2$ and $K_{S_0} = 10^{-4}$. To add dependence on Ri , we compute a least squares fit of K_T and K_S , averaged over $\sigma_{fg}t > 8$ for all simulations,

$$K_T(R_\rho, Ri) = 3.07 \times 10^{-5} R_\rho^{-4.0} Ri^{0.17} \quad \text{and} \quad (16)$$

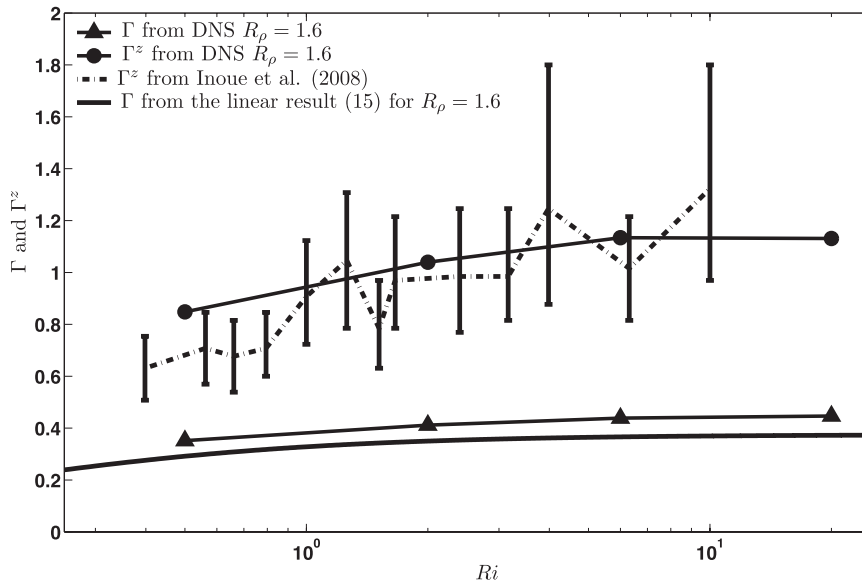


FIG. 9. The Γ and Γ^z for different Ri compared to observations from Inoue et al. (2008). Vertical bars denote 95% confidence limits (Inoue et al. 2008). Mean R_ρ is nearly constant around 1.65 in Inoue et al. (2008).

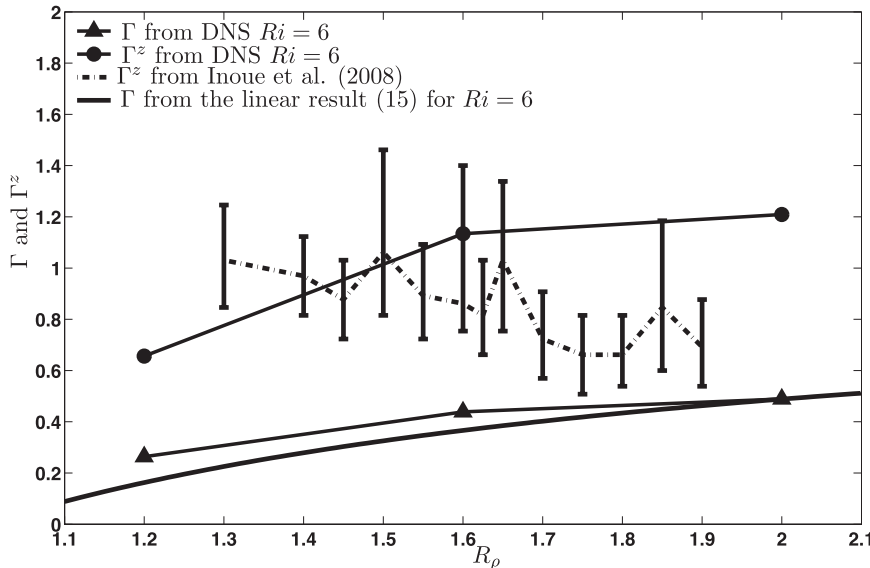


FIG. 10. As in Fig. 9, but for different R_ρ s. Mean Ri ranges between 0.4 and 10 for Inoue et al. (2008).

$$K_S(R_\rho, Ri) = 4.38 \times 10^{-5} R_\rho^{-2.7} Ri^{0.17}. \quad (17)$$

Both K_T and K_S decrease with decreasing Ri (Figs. 11a,c), which is also true in the salt-fingering system with $Ri < 0.25$ described by Smyth and Kimura (2011). This finding was unexpected and has important implications for turbulence modeling, where it is often assumed that, because background shear represents an energy source for mixing, its introduction will increase effective diffusivities (e.g., Large et al. 1994; Zhurbas and Oh 2001; Smyth and Ruddick 2010). The Ri dependence differs significantly from the prediction of Kunze (1994), $K_S \propto Ri^{1.0}$, but is closer to that of Inoue et al. (2008), $K_S \propto Ri^0$ (Fig. 11c).

We also find that K_T and K_S increase with decreasing R_ρ (Figs. 11b,d), which has been reported in previous DNS of two-dimensional salt fingering (W. J. Merryfield and M. Grindler 2000, personal communication; Stern et al. 2001) and laboratory experiments (Turner 1967; Linden 1973; McDougall and Taylor 1984; Taylor and Bucens 1989). Our K_T and K_S are consistent with DNS results of W. J. Merryfield and M. Grindler (2000, personal communication) (Figs. 11b,d). This agreement should be interpreted with caution because of the difference in Ri , τ , and computational domain dimensions. Estimates for three-dimensional salt fingering by Stern et al. (2001) are twice as large; this could be due to the presence of the shear and difference in τ in our simulations (Figs. 11b,d).

In the absence of shear, our K_S (open triangle) is consistent with laboratory experiments (Turner 1967; Linden 1973; Schmitt 1979a) and theoretical prediction (Kunze

1987) (Fig. 12, small symbols and dashed-dotted curve). Likewise, when R_ρ is sufficiently small, the effect of shear is secondary and our results agree with those from the laboratory experiments and theoretical prediction (large solid triangle at $R_\rho = 1.2$). However, when Ri is finite and R_ρ is substantially greater than 1, shear may be expected to have a significant effect. Our DNS results show an overall reduction in K_S in the sheared cases; moreover, the decrease in K_S with increasing R_ρ is amplified. Simulations with higher R_ρ are needed to verify (17) with the laboratory experiments and theoretical prediction (Fig. 12, solid curve).

In two-dimensional unsheared, turbulent salt fingers, Stern et al. (2001) showed that decrease in τ from 0.04 to 0.01 increased the heat flux by 15%. In 3D sheared, turbulent salt fingering, Kimura and Smyth (2007) found that the decrease in τ from 0.04 to 0.01 increases the K_T and K_S by a factor of 2. The effective diffusivities of heat and salt for the ocean may therefore be up to 2 times larger than (16) and (17).

The flux ratio γ_s remains within $\sim 10\%$ of the linear value 0.6 (Fig. 13a). In the sheared, turbulent salt-fingering regime, γ_s is about 8% higher than its linear value for the unsheared case. Ruddick (1985) suggested that individual salt sheets rapidly lose their momentum via lateral diffusion and therefore $Sc < 1$. A laboratory experiment to confirm this hypothesis was inconclusive (Ruddick et al. 1989). Linear stability analysis of salt sheets (Smyth and Kimura 2007) and subsequent DNS (Kimura and Smyth 2007) for a single initial case confirm that $Sc < 1$ for $Ri = 2$. The value of $Sc < 1$ holds for Ri ranging from 0.5 to 20

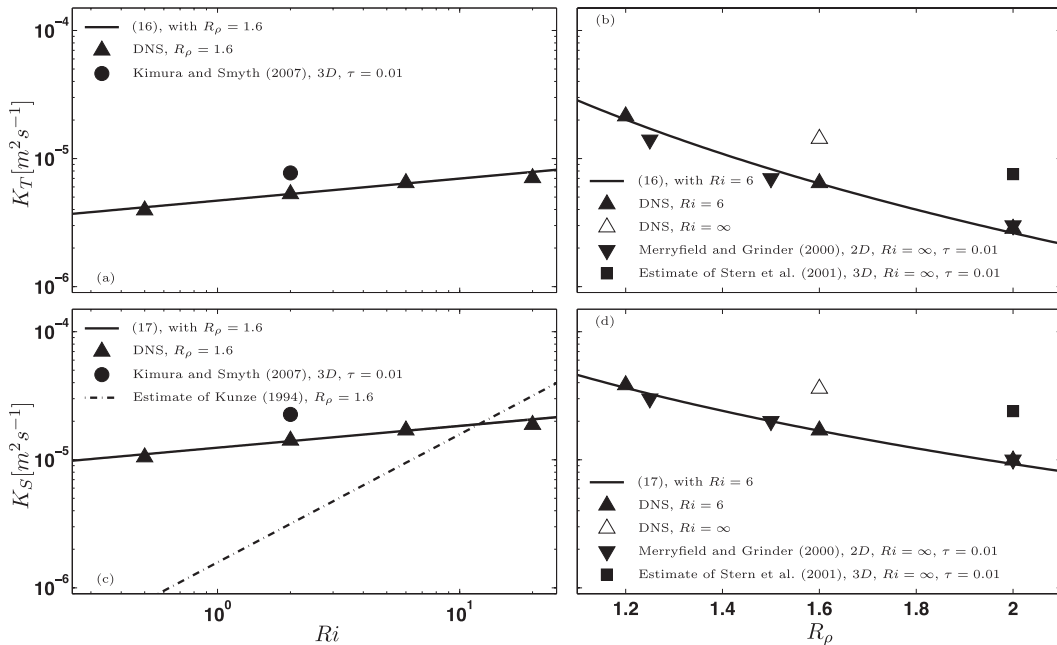


FIG. 11. Effective diffusivity of heat with respect to (a) Ri and (b) R_ρ ; and of salt with respect to (c) Ri and (d) R_ρ . Solid curves represent the parameterizations (16) and (17) with arguments as indicated in the legend. (a),(b) Circles indicate diffusivities from 3D DNS with molecular diffusivity ratio $\tau = 0.01$ (Kimura and Smyth 2007); DNS results presented here have $\tau = 0.04$. (b),(d) Downward triangles indicate 2D DNS results with $Ri = \infty$ and $\tau = 0.01$ (W. J. Merryfield and M. Grinder 2000, personal communication). (b),(d) Squares are effective diffusivities for $Ri = \infty$ (Stern et al. 2001) estimated from the ratio of 2D to 3D fluxes using accessible values of τ and then multiplying the ratio onto directly computed 2D fluxes with $\tau = 0.01$.

(Fig. 13b). The effective diffusivity of the momentum (viscosity) is an order of magnitude smaller than that of salt, confirming (over the simulated range of Ri and R_ρ) that salt sheets are inefficient at transporting momentum.

c. Observational estimates of effective diffusivities

In interpreting observational data, the Osborn and Cox (1972) diffusivity model in conjunction with the isotropy assumption gives

$$K_T^{\chi^2} = \frac{\chi_T^2}{2 \left\langle \left(\frac{\partial B_T}{\partial z} \right)^2 \right\rangle}; \quad K_S^{\chi^2} = \frac{\chi_S^2}{2 \left\langle \left(\frac{\partial B_S}{\partial z} \right)^2 \right\rangle}, \quad (18)$$

based on property variance dissipations, where $\chi_S^2 = 6\kappa_S \langle (\partial b_S / \partial z)^2 \rangle$. These estimates are exact for stationary, homogeneous, isotropic turbulence. Here, we compare these estimates with the true diffusivities K_T and K_S , computed directly using fluxes (12).

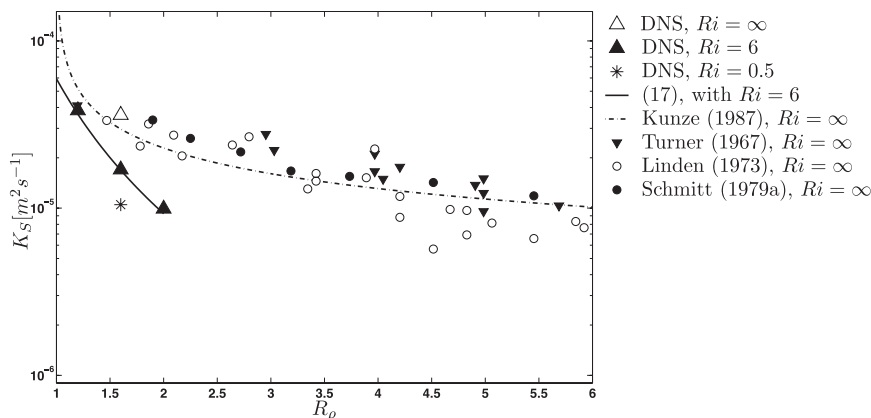


FIG. 12. Effective diffusivity of salt with respect to R_ρ compared to that of theoretical (Kunze 1987) and laboratory (Turner 1967; Linden 1973; Schmitt 1979a) estimates.

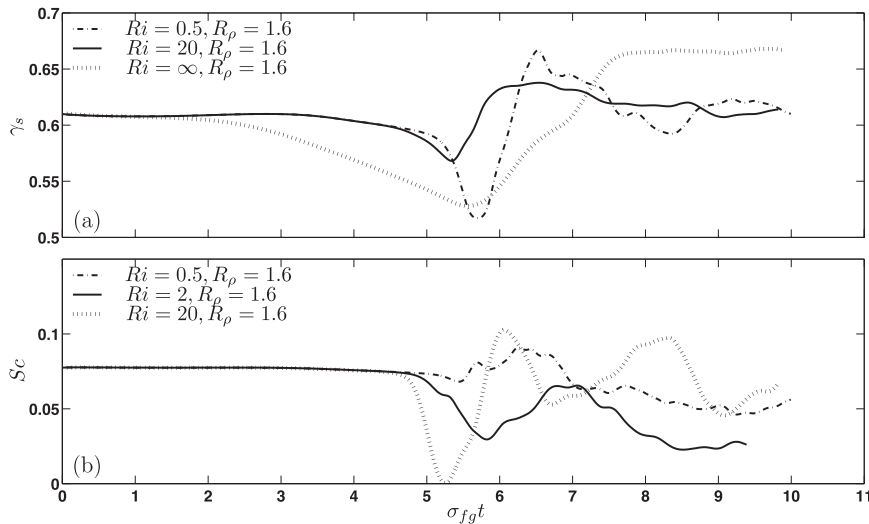


FIG. 13. Evolution of (a) flux ratio γ_s and (b) turbulent Schmidt number Sc with respect to scaled time for different Ri with keeping $R_\rho = 1.6$.

The isotropic Osborn–Cox model (18) captures the R_ρ dependence of K_T and K_S (Figs. 14a,b). Both $K_T^{\chi^c}$ and $K_S^{\chi^c}$ decrease with increasing R_ρ , consistent with the trends of K_T and K_S from DNS and observations by St. Laurent and Schmitt (1999). However, both $K_T^{\chi^c}$ and $K_S^{\chi^c}$ are smaller by up to a factor of 3 than K_T and K_S for the range of R_ρ discussed here (Figs. 14a,b). The isotropy assumption alone cannot explain this difference, because ratios χ_T^z/χ_T and χ_S^z/χ_S range between 0.8 and 1.2 in section 5. The Osborn and Cox (1972) diffusivity model combined with isotropy assumption can underestimate K_T and K_S by up to a factor of 3 for turbulent salt fingering.

6. Conclusions

We have simulated sheared, turbulent salt fingering in a sharp high-gradient interface characteristic of laboratory studies (Turner 1967; Schmitt 1979a; McDougall and Taylor 1984; Taylor 1992). Although these simulations are intended to shed light on oceanic thermohaline staircases, the following caveats should be noted:

- (i) The ratio of molecular diffusivity of salt to heat is 4 times larger than in the real ocean.
- (ii) The interface thickness is at least 3 times smaller than observed thickness of thermohaline staircases. In much thicker layers and continuous stratification, salt-finger flux laws change because fingers no longer extend across the interface from one homogeneous layer to the other (Kunze 1987).
- (iii) The equation of state is linear.

Our main findings are as follows:

- (i) Scalar gradients are nearly isotropic in the dissipation range, but velocity gradients are not. The approximations of ϵ based on vertical shears, which are often used in interpretations of microstructure data, underestimate its value by a factor of 2–3. This suggests that the rate of dissipation by sheared, turbulent salt fingering can be 2–3 times larger than measured inferences.
- (ii) The geometry of the primary instability is often (though not always) reflected in the anisotropy of the turbulent salt-fingering regime.
- (iii) The isotropy assumption can lead to overestimation of the dissipation ratio Γ by a factor of 2 to 3. This will impact estimates of correlation time scales in the k – ϵ model of turbulent salt fingering (e.g., Canuto et al. 2008). It also caused Inoue et al. (2008) to incorrectly ascribe the signals in St. Laurent and Schmitt (1999) to fingers with wavelengths larger than those of the fastest-growing mode.
- (iv) Effective diffusivities of heat and salt can be reduced by either an increase in R_ρ or (surprisingly) a decrease in Ri . Empirical fits give $K_T(R_\rho, Ri) = 3.07 \times 10^{-5} R_\rho^{-4.0} Ri^{0.17}$ and $K_S(R_\rho, Ri) = 4.38 \times 10^{-5} R_\rho^{-2.7} Ri^{0.17}$. Kimura and Smyth (2007) showed that a decrease in τ from 0.04 to 0.01 increased K_T and K_S by a factor of 2. The dependence on Ri differs significantly from the theoretical prediction of Kunze (1994).
- (v) Effective diffusivities estimated by the Osborn and Cox (1972) model with isotropy assumption produced

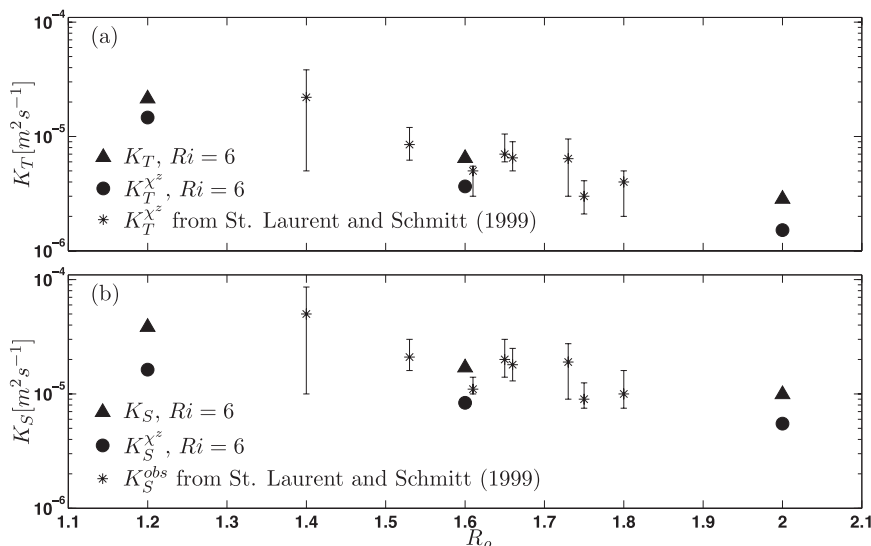


FIG. 14. Comparisons of effective diffusivities of (a) heat and (b) salt with respect to density ratio R_ρ . Because of small-scale structures in salinity, estimation of χ_S from observations is difficult. Thus, K_S in (b) is estimated as $K_S^{\text{obs}} = (R_\rho/\gamma_s)K_T^{\chi_S}$ in the interpretations of observations, where γ_s is the linear theoretical value.

consistent R_ρ dependence but are up to a factor of 3 too small.

- (vi) Values of nondimensional mixing efficiency Γ , flux ratio γ , and Schmidt number Sc in the turbulent salt-fingering regime are predicted by linear theory with remarkable accuracy.

Acknowledgments. Comments from two anonymous reviewers improved the manuscript. Computer time was provided by the National Center for Atmospheric Research (NCAR). The graphics were produced using VAPOR with help from VisLab at NCAR. The work was supported by the National Science Foundation under Grant 0453140.

REFERENCES

- Bryan, F., 1987: On the parameter sensitivity of primitive equation ocean general circulation. *J. Phys. Oceanogr.*, **17**, 970–985.
- Canuto, V., Y. Cheng, and A. Howard, 2008: A new model for double diffusion + turbulence. *Geophys. Res. Lett.*, **35**, L02613, doi:10.1029/2007GL032580.
- Caplan, S., 2008: Microstructure signature of equilibrium double-diffusive convection. M.S. thesis, Naval Postgraduate School, 75 pp.
- Gargett, A. E., and G. Holloway, 1992: Sensitivity of the GFDL ocean model to different diffusivities of heat and salt. *J. Phys. Oceanogr.*, **22**, 1158–1177.
- , T. R. Osborn, and P. W. Nasmyth, 1984: Local isotropy and the decay of turbulence in a stratified fluid. *J. Fluid Mech.*, **144**, 231–280.
- , W. Merryfield, and G. Holloway, 2003: Direct numerical simulation of differential scalar diffusion in three-dimensional stratified turbulence. *J. Phys. Oceanogr.*, **33**, 1758–1782.
- Gregg, M., and T. Sanford, 1987: Shear and turbulence in thermohaline staircases. *Deep-Sea Res.*, **34**, 1689–1696.
- Hamilton, J., M. Lewis, and B. Ruddick, 1989: Vertical fluxes of nitrate associated with salt fingers in the world's oceans. *J. Geophys. Res.*, **94**, 2137–2145.
- Hazel, P., 1972: Numerical studies of the stability of inviscid parallel shear flows. *J. Fluid Mech.*, **51**, 39–62.
- Howard, L., 1961: Note on a paper of John W. Miles. *J. Fluid Mech.*, **10**, 509–512.
- Inoue, R., E. Kunze, L. S. Laurent, R. Schmitt, and J. Toole, 2008: Evaluating salt-fingering theories. *J. Mar. Res.*, **66**, 413–440.
- Itsweire, E., J. Kosefe, D. Briggs, and J. Ferziger, 1993: Turbulence in stratified shear flows: Implications for interpreting shear-induced mixing in the ocean. *J. Fluid Mech.*, **23**, 1508–1522.
- Kimura, S., and W. Smyth, 2007: Direct numerical simulation of salt sheets and turbulence in a double-diffusive shear layer. *Geophys. Res. Lett.*, **34**, L21610, doi:10.1029/2007GL031935.
- Kolmogorov, A., 1941: The local structure of turbulence in incompressible viscous fluid for very large Reynolds number. *Dokl. Akad. Nauk SSSR*, **30**, 301–305.
- Kunze, E., 1987: Limits on growing finite-length salt fingers: A Richardson number constraint. *J. Mar. Res.*, **45**, 533–556.
- , 1990: The evolution of salt fingers in inertial wave shear. *J. Mar. Res.*, **48**, 471–504.
- , 1994: A proposed flux constraint for salt fingers in shear. *J. Mar. Res.*, **52**, 999–1016.
- , 2003: A review of oceanic salt fingering theory. *Prog. Oceanogr.*, **56**, 399–417.
- Lambert, R. B., and W. Sturges, 1977: A thermohaline staircase and vertical mixing in the thermocline. *Deep-Sea Res.*, **24**, 211–222.
- Large, W. G., J. C. McWilliams, and S. C. Doney, 1994: Oceanic vertical mixing: A review and a model with a nonlocal boundary layer parameterization. *Rev. Geophys.*, **32**, 363–403.
- Linden, P., 1973: On the structure of salt fingers. *Deep-Sea Res.*, **20**, 325–340.

- , 1974: Salt fingers in a steady shear flow. *Geophys. Fluid Dyn.*, **6**, 1–27.
- Lueck, R., 1987: Microstructure measurements in a thermohaline staircase. *Deep-Sea Res.*, **34**, 1677–1688.
- McDougall, T. J., and J. R. Taylor, 1984: Flux measurements across a finger interface at low values of the stability ratio. *J. Mar. Res.*, **42**, 1–14.
- , and B. R. Ruddick, 1992: The use of ocean microstructure to quantify both turbulent mixing and salt fingering. *Deep-Sea Res.*, **39**, 1931–1952.
- McEwan, A., 1983: Internal mixing in stratified fluids. *J. Fluid Mech.*, **128**, 59–80.
- Merryfield, W. J., G. Holloway, and A. E. Gargett, 1999: A global ocean model with double-diffusive mixing. *J. Phys. Oceanogr.*, **29**, 1124–1142.
- Miles, J., 1961: On the stability of heterogeneous shear flows. *J. Fluid Mech.*, **10**, 496–508.
- Molcard, R., and R. I. Tait, 1977: The steady state of the step structure in the Tyrrhenian Sea. *A Voyage of Discovery, George Deacon 70th Anniversary Volume*, Pergamon Press, 221–233.
- Moum, J. N., 1996: Efficiency of mixing in the main thermocline. *J. Geophys. Res.*, **101** (C5), 12 057–12 069.
- Nash, J. D., and J. N. Moum, 1999: Estimating salinity variance dissipation rate from conductivity microstructure measurements. *J. Atmos. Oceanic Technol.*, **16**, 263–274.
- Oakey, N. S., 1982: Determination of the rate of dissipation of turbulent energy from simultaneous temperature and velocity shear microstructure measurements. *J. Phys. Oceanogr.*, **12**, 256–271.
- Osborn, T. R., 1980: Estimates of the local rate of vertical diffusion from dissipation measurements. *J. Phys. Oceanogr.*, **10**, 83–89.
- , and C. S. Cox, 1972: Oceanic fine structure. *Geophys. Fluid Dyn.*, **3**, 321–345.
- Ruddick, B. R., 1985: Momentum transport in thermohaline staircases. *J. Geophys. Res.*, **90**, 895–902.
- , R. W. Griffiths, and G. Symonds, 1989: Frictional stress at a sheared double-diffusive interface. *J. Geophys. Res.*, **94**, 18 161–18 173.
- Schmitt, R. W., 1979a: Flux measurements on salt fingers at an interface. *J. Mar. Res.*, **37**, 419–436.
- , 1979b: The growth rate of super-critical salt fingers. *Deep-Sea Res.*, **26A**, 23–44.
- , 1990: On the density ratio balance in the central water. *J. Phys. Oceanogr.*, **20**, 900–906.
- , 1994: Double diffusion in oceanography. *Annu. Rev. Fluid Mech.*, **26**, 255–285.
- , 2003: Observational and laboratory insights into salt finger convection. *Prog. Oceanogr.*, **56**, 419–433.
- , H. Perkins, J. Boyd, and M. Stalcup, 1987: C-SALT: An investigation of the thermohaline staircase in the western tropical North Atlantic. *Deep-Sea Res.*, **34**, 1655–1665.
- Shen, C., 1995: Equilibrium salt-fingering convection. *Phys. Fluids*, **7**, 706–717.
- Smyth, W. D., 2008: Instabilities of a baroclinic, double diffusive frontal zone. *J. Phys. Oceanogr.*, **38**, 840–861.
- , and J. N. Moum, 2000: Anisotropy of turbulence in stably stratified mixing layers. *Phys. Fluids*, **12**, 1327–1342.
- , and S. Kimura, 2007: Instability and diapycnal momentum transport in a double-diffusive stratified shear layer. *J. Phys. Oceanogr.*, **37**, 1551–1565.
- , and B. Ruddick, 2010: Effects of ambient turbulence on interleaving at a baroclinic front. *J. Phys. Oceanogr.*, **40**, 685–712.
- , and S. Kimura, 2011: Mixing in a moderately sheared salt fingering layer. *J. Phys. Oceanogr.*, in press.
- , J. Nash, and J. Moum, 2005: Differential diffusion in breaking Kelvin–Helmholtz billows. *J. Phys. Oceanogr.*, **35**, 1004–1022.
- Stern, M., 1960: The ‘salt fountain’ and thermohaline convection. *Tellus*, **12**, 172–175.
- , 1975: *Ocean Circulation Physics*. Academic Press, 246 pp.
- , T. Radko, and J. Simeonov, 2001: Salt fingers in an unbounded thermocline. *J. Mar. Res.*, **59**, 355–390.
- St. Laurent, L., and R. Schmitt, 1999: The contribution of salt fingers to vertical mixing in the North Atlantic Tracer-Release Experiment. *J. Phys. Oceanogr.*, **29**, 1404–1424.
- Tait, R. I., and M. R. Howe, 1968: Some observations of thermohaline stratification in the deep ocean. *Deep-Sea Res.*, **15**, 275–280.
- Taylor, G. I., 1935: Statistical theory of turbulence. II. *Proc. Roy. Soc. London*, **151A**, 444–454.
- Taylor, J. R., 1992: Anisotropy of salt fingers. *J. Phys. Oceanogr.*, **23**, 554–565.
- , and P. Bucens, 1989: Salt fingers and convecting layers. *Deep-Sea Res.*, **16**, 497–511.
- Toole, J., and D. Georgi, 1981: On the dynamics of double diffusively driven intrusions. *Prog. Oceanogr.*, **10**, 123–145.
- Turner, J., 1967: Salt fingers across a density interface. *Deep-Sea Res.*, **14**, 599–611.
- Walsh, D., and B. Ruddick, 1995: Double diffusive interleaving: The effect of nonconstant diffusivities. *J. Phys. Oceanogr.*, **25**, 348–358.
- , and —, 2000: Double-diffusive interleaving in the presence of turbulence the effect of a nonconstant flux ratio. *J. Phys. Oceanogr.*, **30**, 2231–2245.
- Winters, K., J. MacKinnon, and B. Mills, 2004: A spectral model for process studies of rotating, density-stratified flows. *J. Atmos. Oceanic Technol.*, **21**, 69–94.
- Yoshida, J., and H. Nagashima, 2003: Numerical experiments on salt-finger convection. *Prog. Oceanogr.*, **56**, 435–459.
- You, Y., 2002: A global ocean climatological atlas of the Turner angle: Implications for double diffusion and watermass structure. *Deep-Sea Res.*, **49**, 2075–2093.
- Zhang, J., R. Schmitt, and R. Huang, 1998: Sensitivity of the GFDL Modular Ocean Model to parameterization of double-diffusive processes. *J. Phys. Oceanogr.*, **28**, 589–605.
- Zhurbas, V., and I. S. Oh, 2001: Can turbulence suppress double-diffusively driven interleaving completely? *J. Phys. Oceanogr.*, **31**, 2251–2254.